OPTIMIZATION OF A PROPELLER FAN FOR NOISE AND EFFICIENCY BY USING 3D INVERSE DESIGN METHOD

Luying ZHANG[1], Thien Xuan DINH[2], Kenji KAWAKITA[2],
Alfred RIDDELL[1], Akira GOTO[3], Mehrdad ZANGENEH[4]

[1] *Advanced Design Technology, 80-86 Grays Inn Rd, London WC1X 8NH, UK*

[2] *Advanced Design Technology Japan Co., Ltd. 8F Sannomiya Sky Building, 4-1-14 Isogamidori, Chuo-ku, Kobe, Hyogo, 651-0086, Japan*

[3] *Technologies & Intellectual Property Division, Ebara Corporation 11-1 Haneda Asahi-cho, Ota-ku, Tokyo 144-8510, Japan*

[4] *Department of Mechanical Engineering, University College London, Torrington Place, London, WC1E 7JE, UK*

SUMMARY

In this work, a methodology for propeller fan optimization using the three-dimensional inverse design method is presented. The vortex distribution, the pressure loading on the blade surface and the stacking were varied during the optimization. The blade geometries were obtained from the 3D inverse design calculation, which can explore a large design space with relatively small amount of input parameters. A multi-objective optimization was carried out based on the DOE study to find the balance between conflicting objectives. The aim is to improve the aerodynamic performance while keeping the noise level under control. The performance of the optimized design was verified by both the computational fluid dynamics (CFD) simulations and experimental study.

INTRODUCTION

Propeller fans have wide applications in ventilation and cooling system. It is used to deliver large airflow against the system resistance. The efficiencies of propeller fans are relatively low compared to tube axial fans or vane axial fans, as there is no duct to guide the flow or stator vanes to recover the pressure. On the other hand, there are quite often requirements on compact size and low noise, apart from the requirement on high efficiency. It is a challenging task to design a propeller fan with overall good performance. Compared to axial compressors and turbines used in air propulsion or power generation, the design methods for axial fans are less standardized or documented. Castegnaro [1] provided a historical overview of the aerodynamic design methods for low-speed axial fans. It started from the ancient fans used for ventilation in mining industry, and reviewed the development of axial fans in parallel with the development of aerodynamic theories and methodologies. The classic design methods employ radial equilibrium equation [2] in combination with the continuity equation and the Euler equation for turbomachines. The spanwise vortex (swirl) distribution is a design input and the axial velocity distribution along the span can be analytically solved. Then the isolated airfoil theory or cascade data can be used to design/select the airfoil shape at a number of spanwise locations. Finally, with the stacking

condition defined the 3D blade geometry of the fan is determined. The performance of the fan has to be verified by experiments or CFD analysis. Iterations are needed sometimes to arrive at a satisfying design.

The distribution of vortex is an important design input. Early designs used more 'free vortex' assumption (rV_θ constant along the span). Ruden [3] first discussed the possibility of using non 'free vortex' distribution in 1937. Since then, the forced vortex and arbitrary vortex designs have been investigated. They were found to increase the pressure-rise when there are dimensional constraints [4]. The acoustic performance should also be affected by the vortex distribution. Because the tip clearance vortex is quite often a major source of the noise and the magnitude of the vorticity is related to the spanwise vortex distribution of the fan blade. Wang and Kruyt [5] discussed the optimum vortex distribution in relation to the hub-to-tip ratio of a low pressure fan. Their results showed that the hub backflow can occur to the fans designed with the optimum quadratic and cubic vortex distributions when the hub-to-tip ratio of the fan is low. Additional criteria have to be developed to avoid the backflow. Also, the study didn't include the effect of stacking, which also plays an important role in aerodynamic and acoustic performance. Forward sweep was believed to help reduce the noise level of the fan, compared to radially stacked fan blade [6]. The rapid development in CFD simulations enabled the designers to evaluate the 3D flow field with higher fidelity. Designs with complex stacking and vortex design have been developed not only to satisfy the aerodynamic performance but also to help the noise reduction. Besides, other requirements such as compact size, size standardization, cost and durability can also make the design more challenging. 'Trial-and-error' approach or many design iterations may be needed. Although the 3D CFD analysis provides more detail on the flow field, it is still used more as an analysis tool than a design tool. Especially when the degree of freedom in the design is large, it is time consuming to couple 3D CFD simulations with optimization techniques.

Okamoto et al. [7] applied the 3D inverse design method [8] to a propeller fan design in 2009. By using CFD analysis and rapid prototyping, they investigated the effect of different vortex pattern, stacking condition and blade loading distribution. The results showed that the best design candidate improved the peak efficiency and reduced the aerodynamic noise over a baseline (commercially available) fan. Compared to the conventional design methods (based on radial equilibrium assumption and cascade data), the inverse design method has the advantage of producing more accurate 3D flow field solution when generating the 3D blade geometry. It is a fast approach comparing to 3D CFD simulations, which makes it ideal to be coupled to an optimization workflow. This is particularly advantageous when the degree of freedom in the design space is large. In this paper, a design/optimization workflow for propeller fans is proposed. It is based on the 3D inverse design method and multi-objective genetic optimization algorithm. CFD analysis is only used to verify the design candidates picked from the optimization. A design of experiments (DOE) approach is used first to explore the design space. The optimization constraints and objectives are then selected based on the DOE study. Meanwhile, the noise control is also included in the optimization.

BASELINE DESIGN AND CFD ANALYSIS

The baseline propeller fan design used in this work is the same one as used in Okamoto et al.'s work [7]. Table 1 listed the design specification of the baseline fan.

Table 1: baseline fan design specification

Design RPM	3,000 [rev/min]
Design flow coefficient (ϕ)	0.22
Hub to tip ratio	0.48
Tip clearance	1.0 [mm]

Figure 1 (left) shows the geometry of the fan (5 blades) and the downstream casing and 4 struts. The fan is installed on the wall. The inlet and outlet are connected to open space. There is about 27 degree forward sweep at the trailing edge of the blade. The baseline design is first simulated in steady state CFD simulations. STAR-CCM+ 2302 is used for all the CFD runs. For turbulence closure Menter SST k-Omega turbulence model is selected. The segregated flow solver (SIMPLE scheme) is employed with incompressible flow (constant density) assumption. 2nd-order convection scheme is used. Figure 1 (mid) shows the computational domain used in the numerical simulations. The inlet domain is a hemisphere with a diameter 10 times of the fan shroud

diameter, so that the far field condition is properly set. Total pressure (atmosphere pressure) and flow direction are specified at the inlet boundary. The outlet domain is a cylinder connected to a conical frustum. The diameter of the cylinder is about 9 times of the fan shroud diameter. Mass flow is specified at the outlet boundary. Symmetric boundary condition is applied to the cylindrical and conical surface. Figure 1 (right) shows the mesh detail near the fan. The total number of mesh elements is about 8.6 million, with 4.6 million mesh elements in the fan near field. The fan impeller zone is set to be rotating domain (blue). The rest of the domain is stationary. Between the rotating domain and the stationary domain, the 'internal interface' (frozen rotor) connection is applied. At all solid walls, 'no-slip' wall condition is specified. The average 'Wall Yplus' on the fan and the casing surface is about 0.5. To evaluate the validity of the mesh setup, a 'coarser' and 'finer' mesh (1.8 and 6.8 million in the fan near field respectively) were tested. Both have averaged Yplus below 1.0 following the recommendation for Menter SST k-Omega turbulence model [9]. The results show the variation of predicted pressure rise is below 1 %.

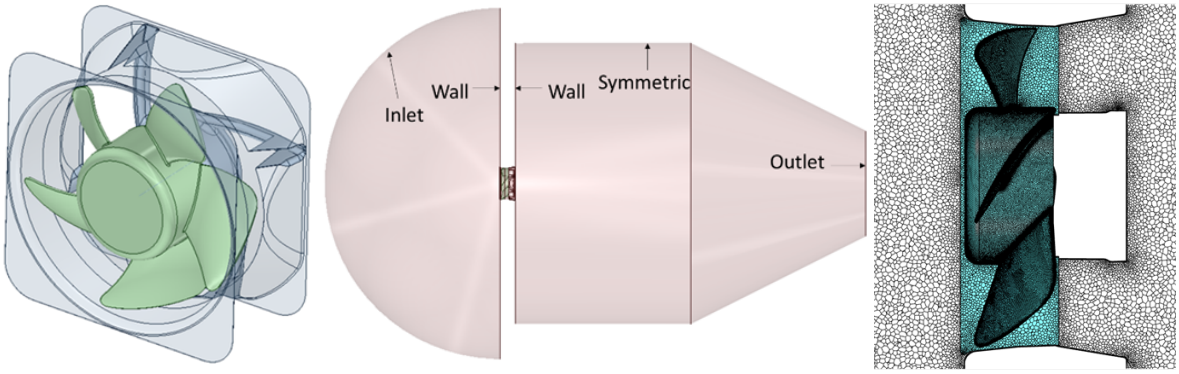

Figure 1: left: baseline design fan geometry; mid: computational domain; right: mesh detail.

Figure 2 (a) shows the predicted fan performance in comparison to the test data. The CFD runs are performed at various flow rates. The result showed a good agreement with the measured pressure rise. As the fan flow rate is reduced, the pressure rise is increased. At flow coefficient about 0.13 there is a drooping of pressure rise, which is also captured by the CFD simulation. At flow coefficient lower than 0.1, the steady CFD simulation starts to show some numerical oscillation. This could be due to the local flow unsteadiness (such as flow separation) not considered in the steady flow assumption. Unsteady CFD simulations tend to perform better in such conditions.

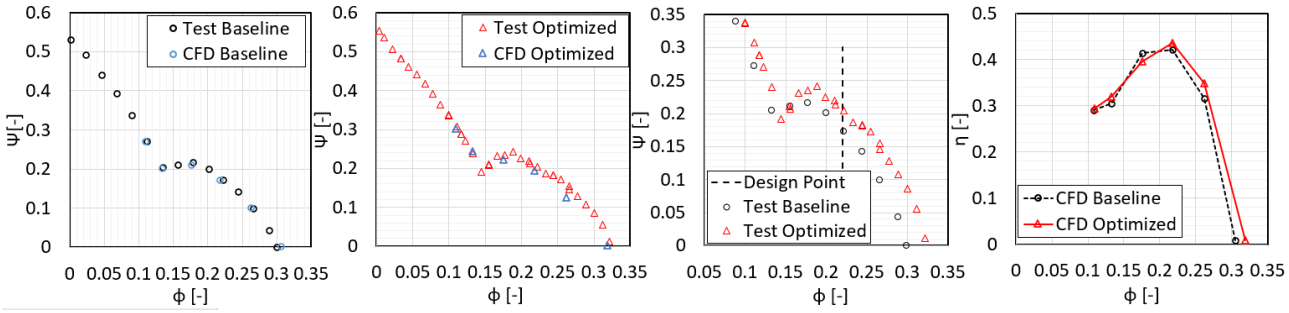

Figure 2: fan performance characteristics [10], a) baseline; b) optimized fan; c) comparison of test; d) comparison of efficiency.

Figure 3 (left) shows the tip clearance flow near the shroud. Helicity is used to highlight the vortex structure. It is defined as the dot product of velocity vector and vorticity vector:

$$H = (\nabla \times \mathbf{W}) \cdot \mathbf{W} \tag{1}$$

The tip leakage vortex filament is largely aligned with the main flow direction so it tends to have higher absolute helicity. Figure 3 (left) shows the contour plot at several different streamwise locations. The high helicity region is caused by the tip clearance flow. It can be seen that near the fan TE the tip clearance flow moves to lower span. It has an impact on both the fan efficiency and the aerodynamic noise. After the numerical scheme is verified, the same meshing strategy and numerical setup are used in all the simulations in the DOE and the optimization study. So, the numerical simulations are consistent between different designs. Meanwhile, the positive helicity is integrated in the fan passage above 60 % span. It is used as a criterion to check the strength of tip clearance vortex flow.

3D INVERSE DESIGN METHOD

For the DOE and optimization work, the design candidates are generated using the 3D inverse design method TURBOdesign1 (TD1) [11]. The method has been described in detail in [8] and has been applied to pumps and compressors designs extensively [12] [13]. In the inverse design method, the specific work across the fan blade is defined by specifying the circumferentially averaged bound circulation:

$$r\overline{V_\theta} = \frac{N}{2\pi}\int_0^{2\pi/N} r \cdot V_\theta d\theta \tag{2}$$

In TD1, $r\overline{V_\theta}$ is normalized by the impeller mean radius (RMS of hub and shroud radius) and the rotational speed. The difference of $r\overline{V_\theta^*}$ (normalized value) between the blade TE and LE will decide the pressure coefficient Ψ ($\frac{\Delta p}{0.5\cdot\rho U_t^2}$, where U_t is the fan tip velocity). Using the isentropic relationship ($\Delta h \cong \frac{\Delta p}{\rho}$)

$$\Psi = \frac{\Delta h}{0.5\cdot U_t^2} \tag{3}$$

Using Euler's equation [14]:

$$\Psi = \frac{\omega(r_2 V_{\theta 2} - r_1 V_{\theta 1})}{0.5\cdot U_t^2} \tag{4}$$

If the inlet flow has no swirl:

$$\Psi = \frac{\omega(r_2 V_{\theta 2})}{0.5\cdot U_t^2} \tag{5}$$

For a fan with fixed speed and dimension, ω and U_t are fixed. The pressure coefficient is determined by the $r\overline{V_\theta}$ distribution at TE, which is equivalent to the vortex distribution. Meanwhile, for incompressible flows, the blade pressure loading (pressure difference across the blade pressure and suction surface) can be linked to $\frac{\partial(r\overline{V_\theta})}{\partial m}$ through:

$$p^+ - p^- = \frac{2\pi}{N}\rho W_{mbl}\frac{\partial(r\overline{V_\theta})}{\partial m} \tag{6}$$

So, the meridional distribution of $\frac{\partial(r\overline{V_\theta})}{\partial m}$ can be used to control the pressure field on the blade surface. The 3D blade geometry is solved according to certain vortex and blade loading specification.

Figure 3 (right) shows the streamwise blade loading definition. It is specified at three spanwise locations: hub, midspan and shroud. At each spanwise location, 4 parameters (NC, ND, SLOPE and DRVT) are needed to define a blade loading curve, which decides the pressure loading on the blade surface. For axial fan application, a fore loaded design generally gives good efficiency. The LE loading (DRVT) is related to the incidence. Normally some positive incidence helps to improve the efficiency but excessive incidence may lead to LE separation or trigger instability at low flow rate conditions. According to Okamoto et al. [7] it is also critical to the diffusion of the tip clearance vortex, which can have a big impact on noise. Finally, the stacking condition can be specified at the fan blade TE, this is done by specifying the wrap angle variation between hub and shroud. Once the spanwise $r\overline{V_\theta^*}$ distribution, the streamwise blade loading and the TE stacking condition are defined, the inverse design solver will solve both the flow field and the corresponding blade geometry, until a convergence is met for both. All three inputs can be varied during DOE and optimization process. The blade thickness is kept the same as the baseline fan.

Figure 4 shows examples of different $r\overline{V_\theta^*}$ distribution (constant, linear and parabolic) at fan TE and their impact on the flow field. All three cases have the same power input. It can be seen that with constant $r\overline{V_\theta^*}$ distribution at TE, the axial velocity (Figure 4 (b)) leaving the fan blade is more uniform. However, the blade loading (Figure 4 (c)) near the hub is very high. This results in high diffusion and blade overturn, which will trigger hub flow separation. With the linear $r\overline{V_\theta^*}$ distribution at TE, the blade loading near the hub is reduced and the diffusion is lower. If the hub $r\overline{V_\theta^*}$ is further reduced as in the parabolic distribution, the hub flow diffusion can be significantly reduced, which helps to avoid the flow separation. However, the axial velocity leaving the fan blade is also much lower at the hub, which may trigger a hub reverse flow. The well-known Strscheletzky criterion of hub backflow [15] was used to check the hub flow condition and to avoid the hub reverse flow in design. But it was deduced for 'free-vortex' (constant $r\overline{V_\theta^*}$) design. In the 3D inverse design

method, the axial velocity is available once the solution is converged. The minimum axial velocity can be monitored during the design and optimization. The spanwise axial velocity distribution also plays an important role in the fan efficiency, as it is related to the flow rate distribution and the leaving kinetic energy at the fan exit. Meanwhile, the diffusion ratio (maximum relative velocity on the blade surface divided by the relative velocity at the trailing edge) can be used to monitor the flow separation triggered by over diffusion. This can be extracted at all spanwise locations. For axial fan design the hub diffusion is quite often the bottle neck.

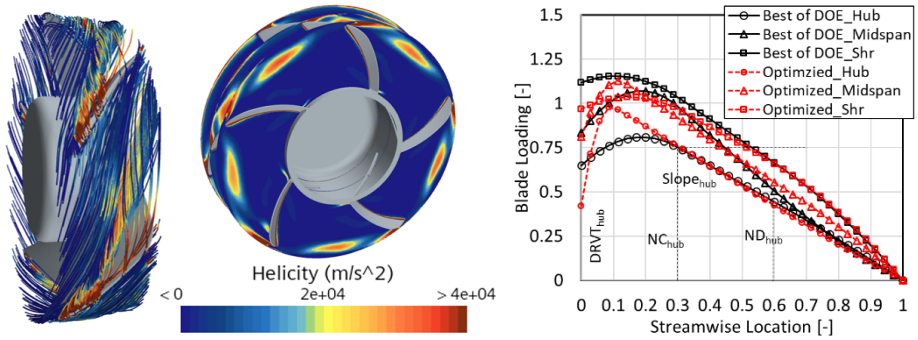

Figure 3: left: helicity distribution in fan passage flow at design condition; right: streamwise blade loading

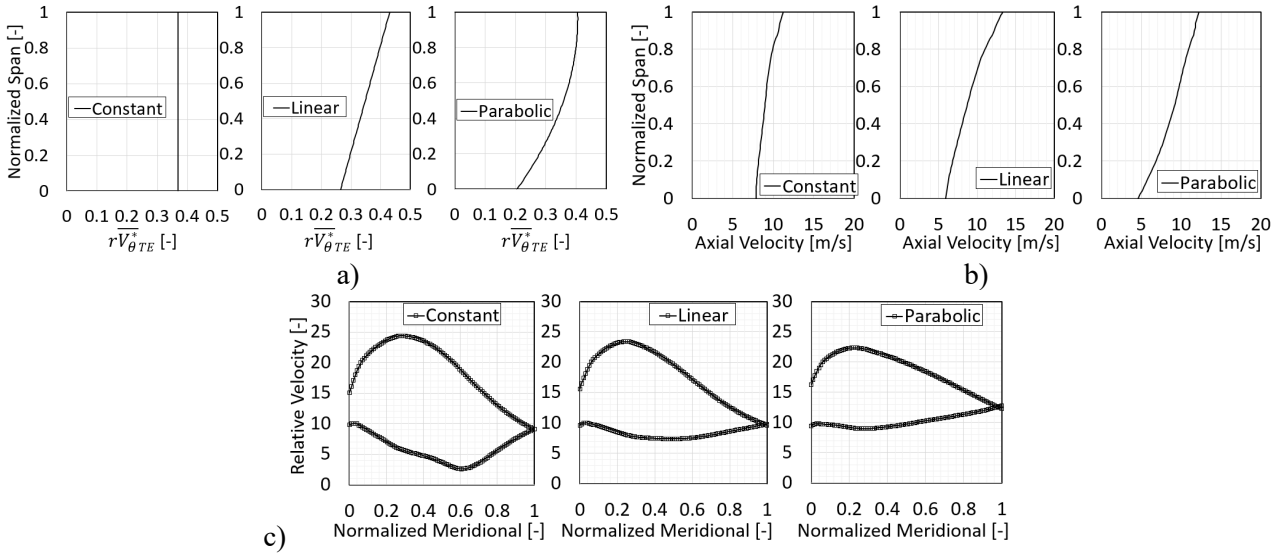

Figure 4: impact of spanwise $r\overline{V_\theta^*}$ distribution;

a) spanwise $r\overline{V_\theta^*}$ distribution at fan TE; b) axial velocity distribution at fan TE; c) isentropic velocity distribution at 10 % span.

DESIGN OF EXPERIMENTS

The DOE candidates are generated by varying the spanwise $r\overline{V_\theta^*}$, the streamwise loading and the stacking at the fan blade TE. The design flow coefficient (0.22) is the same as the baseline fan (shown in Table 1). Parabolic spanwise $r\overline{V_\theta^*}$ and linear stacking at blade TE are assumed. Table 2 shows the range of the variation for each DOE input variable. For the streamwise loading, the slope and DRVT are allowed to vary at three spanwise locations. A Latin hypercube sampling method is used to generate near-random samples in the design space. The design candidates generated have been screened first to rule out poor design candidates. Based on the inverse design solution, designs with blade overturning, local sudden turning or over diffusion on the blade surface are ruled out from the DOE database. 63 design candidates are selected in the end. CFD simulation has been carried out for each design candidate, using the same meshing strategy and numerical setup as mentioned before. The pressure coefficient (Ψ) of most DOE candidates varies between 0.15 and 0.2, with the baseline fan value around 0.172. The efficiency (η) varies between 0.34 and 0.44. The baseline fan efficiency is about 0.42. The relationship between pressure coefficient, fan efficiency and power are plotted in Figure 5 (Linear regression trend line using ordinary least squares approximation and the coefficient of determination (R2) are

plotted for each plot). It can be seen that the fan pressure coefficient is generally higher with higher power input (Figure 5 (a)). However, it is not a strong linear relationship. This is because as the power input is increased the fan efficiency tends to be lower (Figure 5 (b)). The higher power input means higher loading on the fan blade, which may lead to more aerodynamic losses. Meanwhile, the leaving kinetic energy can be higher too, which can also reduce the fan total-to-static efficiency. Figure 5 (c) shows the pressure coefficient is also dependent on the fan efficiency. If the relatively high efficiency cannot be maintained, the increase in power may not lead to higher pressure rise. On the other hand, the efficiency is also strongly related to the throat of the fan (Figure 5 (d)), as the throat can affect the fan speed line characteristics. Both the maximum flow rate and the position of the peak efficiency point are affected by the throat. This means the throat has to be properly constrained during design optimization.

Table 2: DOE input variables

Streamwise blade loading		**Spanwise variables**	
Slope_{hub}	[- 5, -2.5]	$r\overline{V_\theta^*}_{hub}$	[0.185, 0.25]
DRVT_{hub}	[0, 0.75]	$r\overline{V_\theta^*}_{mid}$	[0.325, 0.4]
Slope_{mid}	[-4, 0]	$r\overline{V_\theta^*}_{shr}$	[0.325, 0.405]
DRVT_{mid}	[0.75, 1.25]	Stacking [deg]	[12, 42.5]
Slope_{shr}	[-3, 0]		
DRVT_{shr}	[0.9, 1.5]		

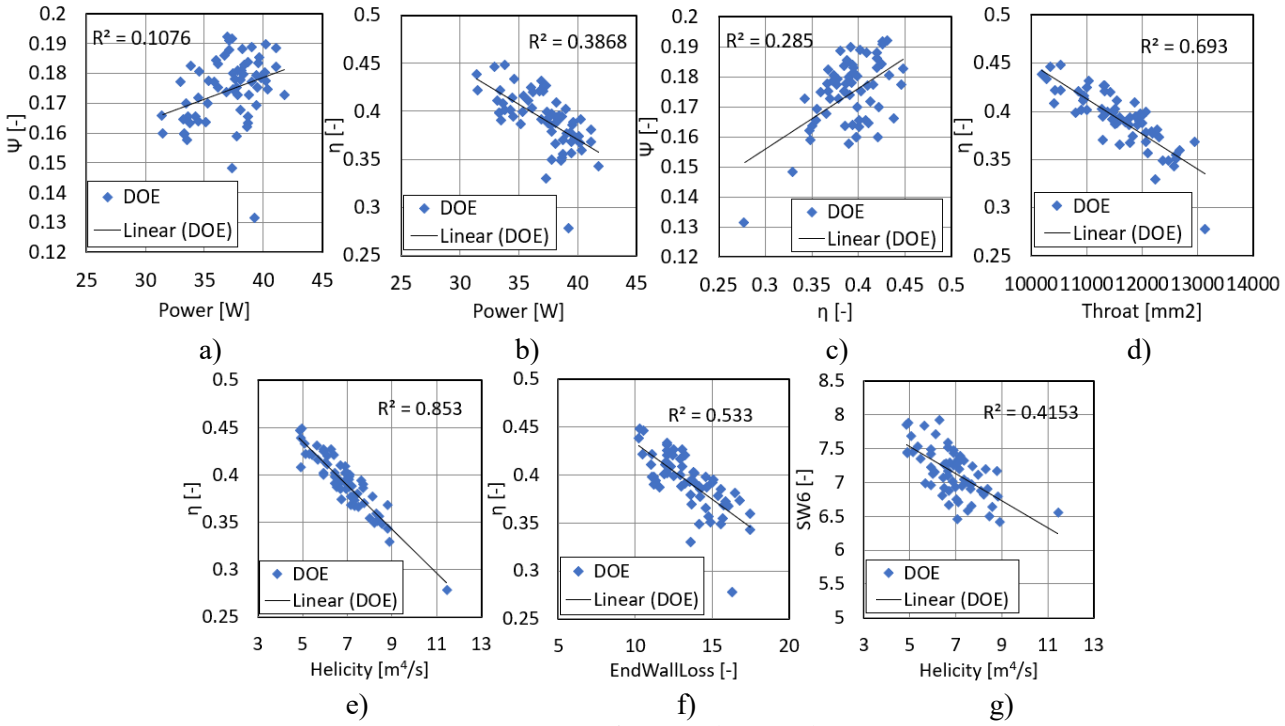

Figure 5: DOE performance data correlation

The efficiency is also plotted against helicity in Figure 5 (e). There is a strong correlation between the two. High helicity tends to cause lower efficiency. Previous study based on test data from [7] also showed high helicity is related to higher acoustic power. Therefore, it is important to control the helicity during design and optimization. Although the inverse design solver doesn't simulate the tip leakage flow directly, the velocity field (near the shroud especially) has an impact on the strength of tip clearance vortex. The fan efficiency against the endwall loss is shown in Figure 5 (f). The endwall loss factor is calculated using the flow field solution from the inverse design solver. According to the loss correlation in [17], the entropy generation near the endwall can be estimated using the velocities near the hub. For low aspect ratio blades, the endwall loss can contribute to a big portion of the overall loss. Figure 5 (f) shows the fan efficiency decreases as the endwall

loss factor is increased. Figure 5 (g) plotted the integrated helicity against 'SW6', which is a parameter calculated from the integration of the zenzicube of the blade surface velocity. It was shown to have correlation to noise level [16] in previous experiments. From Figure 5 (g), it can be observed that the 'SW6' parameter has some correlation with the helicity computed from CFD flow field. It is used in optimization as a parameter to characterize the blade noise.

The performance of the best design candidate from the DOE study is compared to the baseline fan performance in Table 3. The best DOE candidate is picked with the consideration of pressure rise and efficiency. Both are increased compared to the baseline design. The selection has an emphasize on pressure rise. The power input is also increased. As a result, the blade loading is higher and the helicity is higher than the baseline design.

Table 3: performance comparison

	Pressure Coefficient Ψ [-]	Helicity [m4/s]	Efficiency η [-]	Power [W]
Baseline	0.172	4.78	0.421	34.0
Best of DOE	0.192	5.66	0.432	37.0
Optimized	0.195 (13.4 %)	5.51	0.436	37.2

DIRECT OPTIMIZATION

After the DOE study has been completed, a direct optimization is carried out to improve the fan performance. The main target is to increase the pressure rise. Meanwhile the noise level should be kept under control. In the direct optimization, the inverse design solver is coupled to a multi-objective genetic algorithm optimizer (TURBOdesign Optima) [18]. Since each solution converges within a few seconds, hundreds of design candidates can be investigated in a few hours' time using a single core. This enables the designers to explore large degree of freedom in the direct optimization. The optimizer used an initial population of 40 designs which were carried through 40 generations. To avoid converging to only one local solution and to further explore the design space, a crossover probability of 0.9 and mutation probability of 0.9 was used. Figure 6 shows the spanwise $r\overline{V_\theta^*}$ and stacking parameterization used in the optimization. Five control points are used for the spanwise $r\overline{V_\theta^*}$ and four control points are used for the stacking, with cubic spline curve assumed.

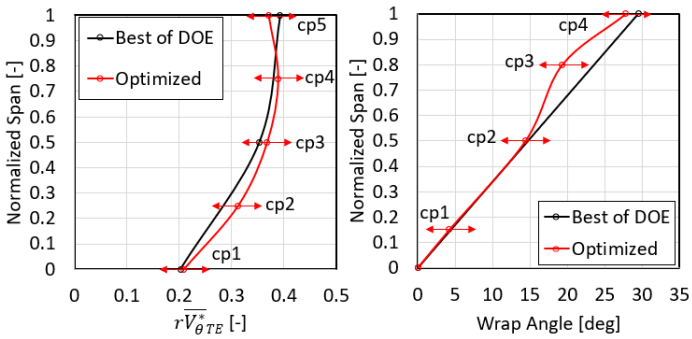

Figure 6: spanwise $r\overline{V_\theta^*}$ and stacking parameterization

Table 4 lists the range of variation for each optimization input. In total, 21 degrees of freedom are allowed. As the DOE analysis showed, it is important to constrain the design space carefully. Since both the flow field and the geometry will be available once the inverse design solution has converged, they can be used as constraints and objectives in the optimization workflow. For the geometry control, it is important to constrain throat, as Figure 5 (d) showed. Over tuning of blade can be ruled out by constraints. For manufacturing purpose, the overlapping between adjacent blades (in the axial view) is also ruled out. For the aerodynamic performance, the power input (from TD1) is constrained so that the power won't be much reduced when varying spanwise $r\overline{V_\theta^*}$. The maximum diffusion ratio is constrained so over diffusion can be avoided. At the blade shroud the local diffusion is also constrained so the shroud loading won't be too high. Because the high shroud loading tends to trigger high loss in the tip clearance region. The blade surface minimum velocity and the minimum axial velocity leaving the blade are constrained to avoid low speed triggered flow separation. Hub backflow mentioned before can also be avoided using these constraints. The maximum deviation is also controlled to be below 20 degrees. The secondary flow factor is related to the hub-to-shroud fluid motion [12]. It is calculated

in the inverse design code by using the velocity difference (downstream of 50 % streamwise location) between the hub and the shroud of the blade. To avoid strong secondary flow, it is also constrained in the optimization. The profile loss factor is computed from the integration of the cube of the blade surface velocity predicted by the inverse design code [17]. It is used to rule out designs with high profile loss. To consider the noise control, the 'SW6' parameter is used. The increase of 'SW6' is limited in the direct optimization. The objectives of the optimization are also listed in Table 4. To optimize for the pressure rise, the power input is maximized. Meanwhile the leaving kinetic energy at the fan TE is minimized. It is defined as the area averaged $\left(\frac{V_2^2}{2}\right)$ at the fan TE from the flow field solution. The leakage loss factor is calculated based on the loss correlation in [17] using the velocities near shroud. It is set to be minimized together with the endwall loss factor in the optimization. With these three objectives, the efficiency will be respected also as an optimization target.

Table 4: optimization setup

Input Variables				**Optimization constraints**			
Blade loading		**Spanwise $r\overline{V_\theta^*}$**		**Aerodynamics**		**Geometry**	
NC_{hub}	[0.1, 0.4]	$r\overline{V_\theta^*}_{cp1}$	[0.175, 0.225]	TD1 Power [W]	[36.5, 38]	Throat [mm^2]	[10500-11000]
ND_{hub}	[0.5, 0.75]	$r\overline{V_\theta^*}_{cp2}$	[0.225, 0.325]	$Diffusion\ Ratio_{max}$	[1.6, 2]	Blade Overlap	none
$Slope_{hub}$	[-4, -2]	$r\overline{V_\theta^*}_{cp3}$	[0.355, 0.405]	$Diffusion\ Ratio_{shr}$	[1.2, 1.475]	$Blade\ Turning_{hub}$ [deg]	[15, 25]
$DRVT_{hub}$	[0, 0.5]	$r\overline{V_\theta^*}_{cp4}$	[0.355, 0.405]	Blade surface min velocity [m/s]	[5, 10]	$Blade\ Turning_{mid}$ [deg]	[15, 35]
NC_{mid}	[0.1, 0.4]	$r\overline{V_\theta^*}_{cp5}$	[0.3, 375]	Min TE axial velocity [m/s]	[3, 7.5]	$Blade\ Turning_{shr}$ [deg]	[5, 15]
ND_{mid}	[0.5, 0.75]	**Stacking [deg]**		Max Deviation [deg]	<20	**Acoustics**	
$Slope_{mid}$	[-4, -2]	$Stacking_{cp1}$	[2, 5.5]	Secondary flow factor	<0.4	SW6	<+2 %
$DRVT_{mid}$	[0.5, 1.0]	$Stacking_{cp2}$	[8.5, 14.5]	Profile loss factor	<0.725	**Optimization Objectives**	
NC_{shr}	[0.1, 0.4]	$Stacking_{cp3}$	[17, 24.5]	TD1 Power [W]	[36.5, 38]	Power	Maximize
ND_{shr}	[0.5, 0.75]	$Stacking_{cp4}$	[27, 34.5]	$Diffusion\ Ratio_{max}$	[1.6, 2]	Leaving kinetic energy	Minimize
$Slope_{shr}$	[-3, -1.25]					Leakage loss	Minimize
$DRVT_{shr}$	[0.75, 1.25]					Endwall loss	Minimize

Figure 7 shows the feasible solutions from the direct optimization. There are 478 solutions that satisfy all the constraints. Figure 7 (left) shows the trade-off between the power and the leaving kinetic energy. The size of the bubbles represents the endwall loss factor. An 'optimized' design is picked considering the balance between multiple objectives. The trade-off between leaving kinetic energy and leakage loss is shown in Figure 7 (right). The selected design has relatively low leaving kinetic energy and leakage loss. The power and endwall loss factor are at medium level among all feasible candidates. Figure 6 (red) shows the spanwise $r\overline{V_\theta^*}$ at fan TE and the stacking distribution of the optimized design. Compared to the best design from DOE, the optimized design reduced the shroud $r\overline{V_\theta^*}$. The increase of power input is done at lower spanwise positions. It also adjusted the stacking at the upper span of the blade. These should help to reduce the loading near the

shroud and may reduce the tip leakage loss. The streamwise blade loading of the optimized design is plotted in Figure 3 (right, red). The optimized design has a fore loaded streamwise loading distribution at hub and midspan. At the shroud the loading is less fore loaded. The LE loading is moderate at hub and midspan. It is bigger at the shroud. So, the fan is designed with some positive incidence in general. The performance of the optimized fan is then verified in the same CFD setup as mentioned before. Table 3 listed the performance parameters. It shows the 'optimized design' further improved the pressure rise and efficiency, in comparison to the best DOE design. It is increase by 13.4 % compared to the baseline. The peak efficiency has been improved by 1.5 %. Meanwhile, the helicity is reduced even when the power is slightly increased in the optimized design.

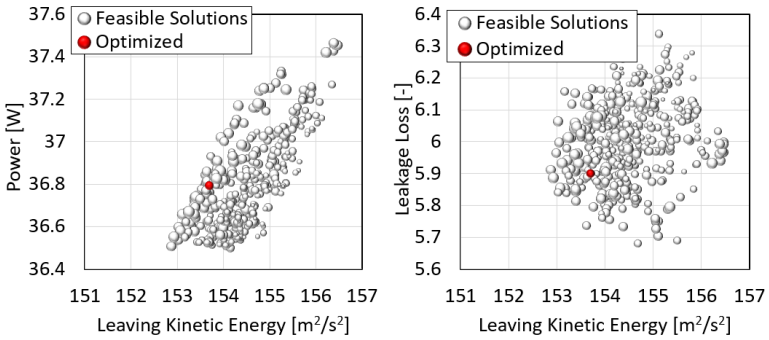

Figure 7: feasible solution from optimization (the size of the bubbles represents the endwall loss factor)

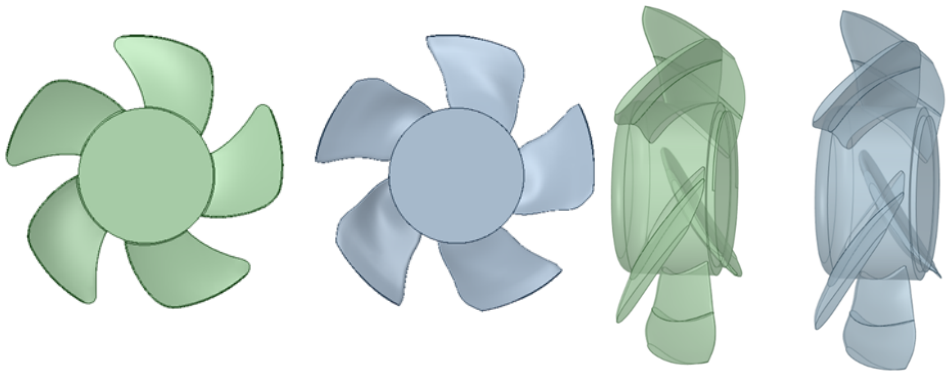

Figure 8: geometry comparison between baseline (green) and optimized design (blue); left: axial view, right: 3D view

The geometry comparison between the optimized design (blue) and the baseline fan (green) is shown in Figure 8. The optimized design increased the blade chord length at hub and shroud. The blade camber is also different between the two along the span. The performance at various flow rates is also computed for the optimized design. The speed line performance is shown and compared to test data in Figure 2 (b). Again, good agreement is achieved between CFD prediction and test data. Figure 2 (c) shows the comparison of test performance between the baseline fan and the optimized design. The results show that the optimized fan has overall higher pressure coefficient. At design condition, the pressure rise is increased by 18.4 %. Meanwhile, the optimized design has not reduced the maximum flow capacity. It is increased by 7.35 % instead, which is also a favored behavior. The calculated efficiency curve is shown in Figure 2 (d). It shows the peak efficiency has been improved by 1.5%, meanwhile the off-design efficiency has not been reduced. The acoustic measurement (Figure 9 (left)) was carried out for both the baseline fan and the optimized design [19]. The 1/2" microphone was placed on the fan center 1 meter upstream from the fan inlet. Figure 9 (right) shows the sound pressure level spectrum at design point. The conditions for frequency analysis of the noise spectrum were: analysis range 0-4 kHz, frequency resolution 2.5 Hz, averaging number 1024 times, and 1600 lines. The flow rates were changed from closed to open and from open to closed. The noise spectrum data was obtained twice under the same flow rate conditions, and the reproducibility of the noise measurement results was confirmed. The blade passing frequency and its multiples are visible in the plot. The cross coupling between the fan blade and the downstream struts also produces a frequency peak. The overall sound pressure level of the optimized design is similar to the baseline fan. On the other hand, since the fan can provide higher pressure rise, it is possible to reduce the rotational speed (from 3000 rpm to 2850 rpm according to Fan Laws) to pass the same amount of flow rate against a fixed system resistance. This reduction of rotational speed can reduce noise level by about 1 dB according to Fan Laws estimation.

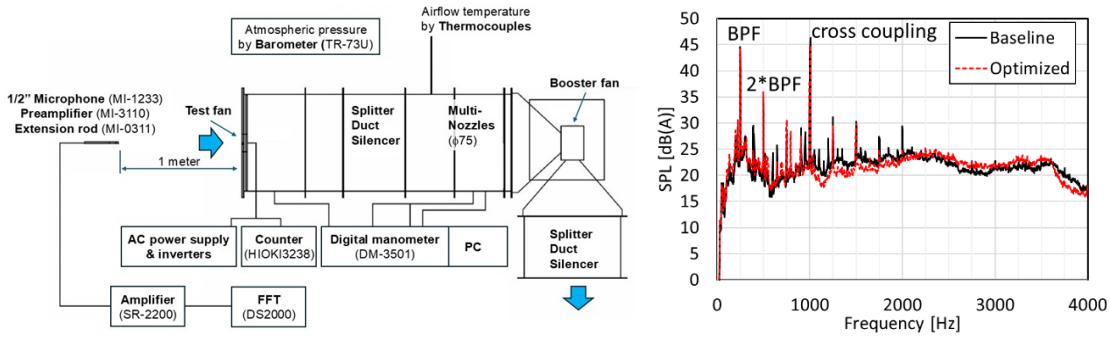

Figure 9: left: experimental facility; right: narrow band frequency spectrum of sound pressure level (A weighting) at ϕ=0.22

CONCLUSION

In this paper, a methodology for propeller fan performance optimization has been developed. The workflow is based on 3D inverse design method and multi-objective optimization algorithm. Both the aerodynamic performance and noise level of the fan can be considered in the optimization process. DOE study was first used to study the sensitivities and dependencies of key input and output parameters. The tendencies were used to guide the direct optimization. The results show that by carefully controlling the flow physics in the fan passage and by using the 3D flow field predicted by the inverse design method, the aerodynamic performance has been improved considerably. This direct optimization workflow is fast and can explore a large design space with complex vortex and stacking distribution. This greatly saves the computational resource compared to CFD solution-based workflow.

ACKNOWLEDGEMENTS

This study has been carried out under the activity of HPP (High-Precision Prediction of Fluid performance and Innovative fluid design) Research Committee of Turbomachinery Society of Japan (TSJ) under the leadership of Prof. Emeritus Chisachi KATO, the University of Tokyo. The authors would like to thank the committee for the permission to publish this work and express sincere gratitude to Prof. Yasumasa SUZUKI, Nihon University, for conducting the performance and noise measurements of the fan.

REFERENCES

[1] Castegnaro, S., "Aerodynamic Design of Low-Speed Axial-Flow Fans: A Historical Overview," Designs, 2(3), p. 20, https://doi.org/10.3390/designs2030020, **2018**

[2] Dixon, S. L., "Fluid Mechanics and Thermodynamics of Turbomachinery," Butterworth Heinemann, London, UK, **1966**

[3] Ruden, P., "Investigation of Single Stage Axial Fans," National Advisory Committee for Aeronautics, Washington, DC, NACA Report No. 1062, **1944**

[4] Castegnaro, S., Masi, M., and Lazzaretto, A., "Preliminary Experimental Assessment of the Performance of Rotor-Only Axial Fans Designed with Different Vortex Criteria," 12th European Conference on Turbomachinery Fluid Dynamics & Thermodynamics, European Turbomachinery Society, Stockholm, Sweden, Apr. 3–7, Paper No. ETC2017-055, **2017**

[5] Wang, J., Kruyt, N., P., "Design for High Efficiency of Low-Pressure Axial Fans with Small Hub-to-Tip Diameter Ratio by the Vortex Distribution Method," J. Fluids Eng. Aug 2022, 144(8): 081201 (15 pages), Paper No: FE-21-1598, https://doi.org/10.1115/1.4053555, **2022**

[6] Wright, T., Simmons, W. E., "Blade Sweep for Low-Speed Axial Fans," J. Turbomach. 112(1): 151-158 (8 pages), https://doi.org/10.1115/1.2927413, **Jan 1990**

[7] Okamoto, H., Goto, A., Furukawa, M., "Design of a Propeller Fan Using 3-D Inverse Design Method and CFD for High Efficiency and Low Aerodynamic Noise," ASME 2009 Fluids Engineering Division Summer Meeting, August 2–6, 2009, Vail, Colorado, USA, Paper No: FEDSM2009-78454, pp. 165-171; 7 pages, https://doi.org/10.1115/FEDSM2009-78454, **2009**

[8] Zangeneh, M., "A compressible three-dimensional design method for radial and mixed flow turbomachinery blades," International Journal for Numerical Methods in Fluids, 13 (5) 599 - 624, 1991. https://doi.org/10.1002/fld.1650130505, **1991**

[9] Menter, F. R., Kuntz, M., and Langtry, R., "Ten Years of Industrial Experience with the SST Turbulence Model," Turbulence, Heat and Mass Transfer 4, ed: K. Hanjalic, Y. Nagano, and M. Tummers, Begell House, Inc., 2003, pp. 625 – 632, **2003**

[10] Courtesy of the HPP (High-Precision Prediction of Fluid performance and Innovative fluid design) Research Committee, Turbomachinery Society of Japan, **2023**

[11] TURBOdesign1, Version 2023.1, Advanced Design Technology Ltd. London, UK, **2023**

[12] Zangeneh, M., Goto, A., and Harada, H., "On the Design Criteria for Suppression of Secondary Flows in Centrifugal and Mixed-Flow Impellers," ASME Journal of Turbomachinery, Vol.120, pp723-735, **1998**

[13] Goto, A. and Zangeneh, M., "Hydrodynamic Design of Pump Diffuser Using Inverse Design Method and CFD," ASME Journal of Fluids Engineering, Vol. 124, pp. 319-328, **2002**

[14] Euler, L., "Maximes Pour Arranger Le Plus Avantageusement Les Machines Destinées À Elever De L'eau Par Le Moyen Des Pompes," (Maxims for arranging most advantageously machines intended to raise water by means of pumps), Mémoires de l'Académie Royale des Sciences et des Belles Lettres à Berlin, 8: 185-232, **1752**

[15] Strscheletzky, M., "Gleichgewichtsformen Der Rotationssymmetrischen Strömungen Mit Konstantem Drall in Geraden, Zylindrischen Rotation-shohlräumen (in German)," Voith Forsch. Konstr., 5, p. 1., **1959**

[16] Consortium for Fan noise reduction technology development, Final report (November 2004), in Japanese, **2004**

[17] Denton, J. D., "Loss Mechanisms in Turbomachines," the 1993 IGTI Scholar Lecture, Ohio USA, Journal of Turbomachinery 115(4), 621-656., **1993**

[18] TURBOdesign Suite, Version 2023.1, Advanced Design Technology Ltd. London, UK, **2023**

[19] Japanese Industrial Standard, JIS B 8330:2000 (Testing methods for turbo-fans), **2000**